



A Wide and Deep Exploration of Radio Galaxies with Subaru HSC (WERGS). I. The Optical Counterparts of FIRST Radio Sources

Takuji Yamashita¹, Tohru Nagao¹, Masayuki Akiyama², Wanqiu He², Hiroyuki Ikeda³, Masayuki Tanaka³,
Mana Niida⁴, Masaru Kajisawa^{1,4}, Yoshiki Matsuoka¹, Kodai Nobuhara⁴, Chien-Hsiu Lee^{5,6}, Tomoki Morokuma⁷,
Yoshiki Toba^{1,8,9}, Toshihiro Kawaguchi¹⁰, and Akatoki Noboriguchi⁴

¹ Research Center for Space and Cosmic Evolution, Ehime University, 2-5 Bunkyo-cho, Matsuyama, Ehime 790-8577, Japan; takuji@cosmos.phys.sci.ehime-u.ac.jp

² Astronomical Institute, Tohoku University, 6-3 Aramaki, Aoba-ku, Sendai, Miyagi 980-8578, Japan

³ National Astronomical Observatory of Japan, 2-21-1 Osawa, Mitaka, Tokyo 181-8588, Japan

⁴ Graduate School of Science and Engineering, Ehime University, Bunkyo-cho, Matsuyama, Ehime 790-8577, Japan

⁵ Subaru Telescope, National Astronomical Observatory of Japan, 650 North Aohoku Place, Hilo, HI 96720, USA

⁶ National Optical Astronomy Observatory, 950 N. Cherry Ave., Tucson, AZ 85719, USA

⁷ Institute of Astronomy, Graduate School of Science, University of Tokyo, 2-21-1 Osawa, Mitaka, Tokyo 181-0015, Japan

⁸ Department of Astronomy, Kyoto University, Kitashirakawa-Oiwake-cho, Sakyo-ku, Kyoto 606-8502, Japan

⁹ Academia Sinica Institute of Astronomy and Astrophysics, P.O. Box 23-141, Taipei 10617, Taiwan

¹⁰ Department of Economics, Management and Information Science, Onomichi City University, Onomichi, Hiroshima 722-8506, Japan

Received 2018 April 10; revised 2018 September 1; accepted 2018 September 12; published 2018 October 23

Abstract

We report the result of optical identifications of FIRST radio sources with the Hyper Suprime-Cam Subaru Strategic Program survey (HSC-SSP). The positional cross-match within $1''$ between the FIRST and HSC-SSP catalogs ($i \lesssim 26$) produced more than 3600 optical counterparts in the 156 deg^2 of the HSC-SSP field. The matched counterparts account for more than 50% of the FIRST sources in the search field, which substantially exceed previously reported fractions of SDSS counterparts ($i \lesssim 22$) of $\sim 30\%$. Among the matched sample, 9% are optically unresolved sources such as radio-loud quasars. The optically faint ($i > 21$) radio galaxies (RGs) show that the fitting linear function of the 1.4 GHz source counts has a slope that is flatter than that of the bright RGs, while optically faint radio quasars show a slope steeper than that of bright radio quasars. The optically faint RGs show a flat slope in the i -band number counts down to 24 mag, implying either less massive or distant radio-active galactic nuclei (AGNs) beyond 24 mag. The photometric redshift and the comparison of colors with the galaxy models show that most of the matched RGs are distributed at redshifts from 0 to 1.5. The optically faint sample includes the high radio-loudness sources that are not seen in the optically bright sample. Such sources are located at redshift $z > 1$. This study gives ~ 1500 radio AGNs lying at the optically faint end and high-redshift regime not probed by previous searches.

Key words: galaxies: active – methods: statistical – radio continuum: galaxies – surveys

1. Introduction

Radio galaxies (RGs), as well as radio-loud active galactic nuclei (AGNs) themselves, will provide us with great opportunities for understanding galaxy formation and evolution. RGs prefer massive host galaxies (stellar mass of more than $10^{11} M_\odot$; Seymour et al. 2007). The powerful radio jets from RGs can drive AGN feedback to regulate star formation in massive host galaxies (McNamara et al. 2005; Fabian 2012; Morganti et al. 2013). Thus, RGs are thought to be a key population in the formation of massive galaxies. Moreover, high- z RGs ($z > 2$) could be a valuable beacon to find protoclusters, because high- z RGs tend to reside in overdensity regions (McCarthy 1993; Miley & De Breuck 2008). In this paper, RGs are defined as radio-loud galaxies with rest-frame 1.4 GHz radio luminosities of $> 10^{24} \text{ W Hz}^{-1}$ (Tadhunter 2016) and optically unresolved morphologies, while radio-loud quasars are optically unresolved objects satisfying the same criterion as the radio luminosity. We refer to both RGs and radio-loud quasars as radio AGNs.

The bright radio radiation of RGs is advantageous for probing high- z AGNs. Such radio sources should be found by wide-area surveys in radio wavelengths (NVSS, Condon et al. 1998; FIRST, Becker et al. 1995; Helfand et al. 2015; SUMSS, Bock et al. 1999; TGSS ADR, Intema et al. 2017),

which follows the pioneering Cambridge Catalog series (e.g., Edge et al. 1959). It is greatly helpful to identify optical counterparts of radio sources to investigate the properties of host galaxies and the optical emission of AGNs.

The Sloan Digital Sky Survey (SDSS; York et al. 2000) allowed identifications of the optical counterparts of radio sources, taking advantage of its large sky coverage. Ivezić et al. (2002) and subsequently Helfand et al. (2015) performed the positional cross-match between the SDSS and FIRST catalogs and identified SDSS counterparts only for $\sim 30\%$ of the FIRST radio core sources. Even though radio sources with an extended complex radio morphology, which are a minority in all the FIRST sources ($\sim 10\%$; Ivezić et al. 2002), were taken into consideration, the matching fraction of the SDSS objects with FIRST sources did not improve (e.g., Ching et al. 2017). This means that more than half of all the FIRST sources do not have SDSS counterparts. This is likely due to the shallow optical sensitivities of SDSS imaging ($r < 22.2 \text{ mag}$).

In fact, a deep optical survey in the VVDS 1 deg^2 field showed that more than half of radio sources with a flux of $> 1 \text{ mJy}$ in 1.4 GHz, which is the same level as the FIRST sensitivity, match optically faint counterparts with $I > 22.9 \text{ mag}$ (Ciliegi et al. 2005). In a 1.4 GHz VLA survey in the 1.3 deg^2 SXDF, Simpson et al. (2006, 2012) found a few hundred optical counterparts of high- z radio AGNs with

$i' < 26$ mag up to $z \sim 4$. Recently, Smolčić et al. (2017a, 2017b) performed 3 GHz VLA deep imaging and reported more than a thousand radio AGNs with <26 mag in the optical bands, up to $z \sim 5$ in the 2.6 deg^2 COSMOS field. Williams et al. (2018) performed an identification of radio sources in the deep 150 MHz LOFAR observation with I -band-selected objects ($I < 24$), and they reported ~ 2000 RGs up to $z \sim 2$ in 9.2 deg^2 of the Boötes field. The previous deep optical surveys in the radio survey regions have successfully identified high- z radio AGNs, but the number of radio AGNs, in particular for high radio luminosity sources, is limited to a few hundred due to their small survey areas of typically $<10 \text{ deg}^2$. The Hyper Suprime-Cam (HSC) Subaru strategic program (SSP; Aihara et al. 2018a) reaches a limiting magnitude of 25.9 in the i -band in a 1400 deg^2 area, thus providing a key combination for identifying rare and faint objects such as radio AGNs.

This paper presents a new exploration for radio AGNs using a combination of the wide and deep optical catalog of the Subaru HSC-SSP and the wide-field radio catalog of FIRST. This exploration is carried out by an ongoing project, WERGS (a Wide and Deep Exploration of RGs with Subaru HSC). In this paper, we particularly focus on the optical and radio properties of RGs discovered in this project. We refer to radio loudness, \mathcal{R} , which is a measure of the radio activity of AGNs. We use radio loudness as an observable value, which is defined as the ratio of the 1.4 GHz flux to the HSC band flux. Radio loudness is typically defined as a ratio of the 5 GHz flux to the B -band flux derived from AGN emission, where AGNs and quasars with $\log \mathcal{R} > 1$ are considered to be radio-loud (Kellermann et al. 1989). Because the HSC band flux is assumed to be dominated by a host galaxy of an RG, the radio loudness in this study could be underestimated. This paper is organized as follows. We introduce the two catalog data sets in Section 2. The method and statistical results of a cross-match between the catalogs are presented in Section 3. The optical and radio properties of the entire HSC-FIRST radio AGN sample are shown in Section 4. The properties of optically faint RGs are discussed in Section 5. A summary is presented in Section 6. Throughout this paper, we use the AB magnitude system and a Λ CDM cosmological model with $H_0 = 70 \text{ km s}^{-1} \text{ Mpc}^{-1}$, $\Omega_M = 0.27$, and $\Omega_\Lambda = 0.73$.

2. The Data

This search for radio AGNs is based on the positional cross-match between the HSC-SSP optical source catalog and the FIRST radio source catalog. In this section, the two source catalogs are described.

2.1. Subaru HSC Survey

The HSC-SSP is a multiband (five broadband filters, g , r , i , z , and y , and four narrowband filters) imaging survey with HSC (Furusawa et al. 2018; S. Kawanomoto et al. 2018, in preparation; Komiyama et al. 2018; Miyazaki et al. 2018) installed on the Subaru 8.2 m telescope. Three complementary layers—the Wide, the Deep, and the UltraDeep—are included in the survey. These layers are different from each other in area and depth.

We utilized the broadband forced photometry catalogs of the early data products internally released as S16A (Aihara et al. 2018b), which were obtained by observations from

2014 March to 2016 January. The typical seeing is $\sim 0''.6$ in the i -band. The astrometric uncertainty is ~ 40 mas in rms according to the comparison with the Pan-STARRS1 Surveys. The forced photometry of each band image is performed using position and shape parameters determined in a reference band. The highest priority band of a reference band is the i -band, followed in order by r , z , y , and g (see Bosch et al. 2018 for more details). We used the two extremes of the survey layers: the Wide layer originally covering 456 deg^2 with a 5σ depth for point sources of $i = 26.4$, and the UltraDeep layer of 4 deg^2 with a depth of $i = 27.0$ (Aihara et al. 2018b). The saturation magnitudes for point sources are 18.4 and 18.7 in the i -band for the Wide layer and the UltraDeep layer, respectively. Using the two extreme layers, we investigate the dependence of the rate of optical identification on the depth of optical imaging. We do not use the Deep layer because the imaging depth of the S16A Deep layer data is as shallow as that of the S16A Wide layer due to incomplete observation in the Deep layer. The Wide layer is composed of six distinct areas, and the UltraDeep layer has two areas, the UD-COSMOS and the UD-SXDS. Because the UD-SXDS area in the S16A data has a shallower depth (10%–40%) than that of the UD-COSMOS, we use only the UD-COSMOS out of the UltraDeep layer. The detailed properties and the data process of the early data products are described in Aihara et al. (2018b) and Bosch et al. (2018).

We produced two clean HSC-SSP samples of the HSC-SSP Wide and UltraDeep layers from the original HSC-SSP forced catalogs in order to exclude detector edges with low sensitivities and junk sources from the original catalogs. Here, we use cModel magnitudes from HSC-SSP photometry and corrected them for Galactic extinction (Schlegel et al. 1998). First, we masked the edges of each area. Around the edges, the number of visits at an object position is much smaller than that in the central regions. The coordinates of the consequent areas after masking the edges are shown in Table 1. Additionally, we removed coadded patches with poor modeling of the PSF due to extremely good seeings (see Section 5.8.4 in Aihara et al. 2018b for details). A patch is the minimum unit of images for data processing. The removed patches have color offsets larger than 0.075 mag from the stellar sequence in the color-color planes of either $g - r$ and $r - i$, $r - i$ and $i - z$, or $i - z$ and $z - y$ (Akiyama et al. 2018; He et al. 2018). We also removed subregions in two patches in the XMM area, where some cModel photometries are significantly over-estimated compared with aperture photometries.

Then, we imposed the following criteria: (i) the number of visits at an object position (`countinputs`) is greater than or equal to 3 (5) for the g and r (i , z , and y) bands in the Wide layer to ensure an observing depth of more than a certain sensitivity, and greater than or equal to 14, 26, and 42 for g and r , i and z , and y , respectively, in the UD-COSMOS; (ii) the central 3×3 pixels of an object are not affected by nearby bright objects (`flags_pixel_bright_object_center=False`; see Coupon et al. 2018 for details); (iii) an object is not deblended further (`deblend_nchild=0`); (iv) an object is a unique source (`detect_is_primary=True`); (v) the central 3×3 pixels of an object are not saturated (`flags_pixel_saturated_center=False`) and (vi) not affected by cosmic rays (`flags_pixel_cr_center=False`); and (vii) an object is not at the edge of a CCD or a coadded patch (`flags_pixel_edge=False`). The following conditions were imposed only for the r , i , and z bands:

Table 1

Defined Coordinates (J2000.0) of Each HSC-SSP Wide Area in Our Survey

Field	Coordinates ^a (deg)	
	$[\alpha(\min), \alpha(\max)]$	$[\delta(\min), \delta(\max)]$
GAMA15H	[210.80, 224.90]	[−1.40, 1.08]
VVDS	[331.20, 336.15]	[−0.45, 1.48]
GAMA09H	[129.05, 135.45]	[−0.20, 2.26]
	[135.45, 139.15]	[−1.15, 2.89]
	[139.15, 140.40]	[−0.55, 2.89]
	[138.64, 140.40]	[2.89, 4.45]
XMM	[29.80, 38.53]	[−6.05, −2.55]
HECTOMAP	[237.08, 247.64]	[42.40, 44.35]
WIDE12H	[176.53, 182.51]	[−14.40, 1.07]

Note.

^a The coordinates of each area are represented by $\alpha(\min) \leq \alpha \leq \alpha(\max)$ and $\delta(\min) \leq \delta \leq \delta(\max)$.

(viii) there are no problems with measuring the cModel flux (cmodel_flux_flags=False) and (ix) centroid positions (centroid_sdss_flags=False), and (x) a signal-to-noise ratio (S/N) of an object is higher than 5 in all three bands. As a result, 23,795,523 sources in a 154 deg² area and 643,932 sources in a 1.78 deg² area are selected as the clean HSC-SSP samples of the Wide layer and the UD-COSMOS, respectively.

2.2. FIRST Radio Survey

The FIRST survey (the Faint Images of the Radio Sky at Twenty-cm; Becker et al. 1995) is a wide-field survey with the Very Large Array (VLA) at 1.4 GHz. The spatial resolution is 5''4, and the statistical astrometry error is 0''2 for bright and compact sources (White et al. 1997). The sky coverage is 10,575 deg², which nearly covers the full SDSS sky area. The wide coverage and the high spatial resolution of FIRST are appropriate for finding a large number of optical counterparts of radio sources. The FIRST detection limit is 1 mJy in 5 σ sensitivity, although in a region at the equatorial strip the limit is only 0.75 mJy. Radio sources detected with a radio flux of more than the FIRST detection limit at a redshift $z \gtrsim 0.5$ meet the definition of radio AGNs, where a radio AGN should have a 1.4 GHz luminosity of $L_{1.4 \text{ GHz}} > 10^{24} \text{ W Hz}^{-1}$ (Tadhunter 2016).

We use the final release catalog of FIRST (Helfand et al. 2015). To produce a uniform sample, we use only sources with a radio flux of more than 1 mJy. The FIRST catalog gives a probability $P(S)$ that a source is a spurious detection near a bright source. We employed the probability and use only sources with $P(S) < 0.05$. Consequently, the FIRST clean samples in the unmasked regions of the HSC-SSP Wide layer and UD-COSMOS layer have 7072 and 106 sources, respectively. See the Appendix for details about how to count FIRST sources in the unmasked HSC-SSP regions.

3. HSC-FIRST Radio Sources**3.1. Positional Matching**

An HSC-SSP counterpart of a FIRST source is identified via nearest neighbor matching between the HSC-SSP *i*-band and FIRST source positions. The search radius r_s is set to be 1''0 for both cross-matching in the Wide and UD-COSMOS layers, because $r_s = 1''0$ is an optimal condition according to an

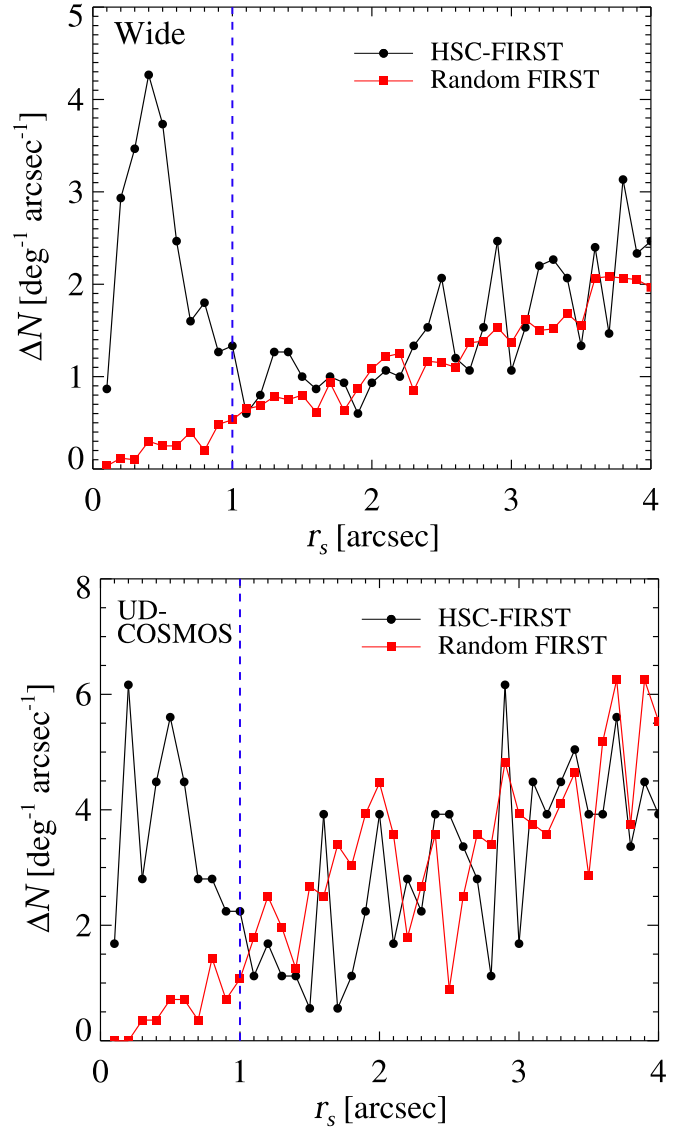


Figure 1. Differential distribution of the separation between the HSC-SSP and FIRST sources. The red points represent the test results of the chance coincidence matches, which were performed using the mock FIRST catalogs with random positions. The blue dashed lines denote the adopted radius of 1''0. (Top) The Wide layer, (bottom) UD-COSMOS.

analysis of the completeness and contamination of the cross-match as discussed below. In Figure 1, the differential distributions of the separation between the HSC-SSP and FIRST sources are compared with those of chance coincidence matches. These examinations were performed in the central 15 deg² region of the GAMA09H Wide layer and the central 0.7 deg² region of the UD-COSMOS. The matches by chance coincidence are estimated from the average numbers of the matches with the mock FIRST catalogs with random positions. Each of the mock catalogs was generated by shifting the FIRST source positions from the original positions to $\pm 1^\circ$ or $\pm 2^\circ$ along the R.A. direction for the Wide layer, to $\pm 0^\circ 1$, $\pm 0^\circ 2$, $\pm 0^\circ 3$, or $\pm 0^\circ 4$ for the UD-COSMOS. The numbers of matches have peaks at $0''0 < r_s < 1''0$ in both of the Wide and the UD-COSMOS layers. Then, at $r_s > 1''0$, the matches gradually increase with increasing radius, approaching the number of random matches. Thus, the matched sources are dominated by chance

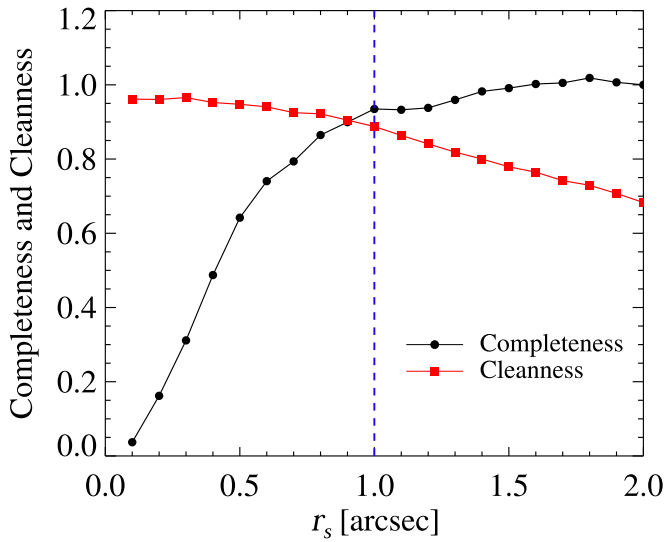


Figure 2. Cumulative distribution of completeness (black) and cleanliness (red) within each searching radius in the Wide layer. The blue broken line indicates the adopted radius of $1''.0$.

coincidence at the radius of more than $1''.0$. It is worth mentioning that 31% of the FIRST sources with HSC counterparts within $1''.0$ in the Wide layer have multiple HSC sources (one to five sources) within the FIRST beam ($2''.7$ radius). Among these multiple HSC sources, except for those HSC sources closest to a FIRST position, 97% have separations larger than $1''.0$, and thus can be attributed to the chance coincidence.

We did not apply any particular algorithm intended for complex and extended radio sources to our cross-match. About only 10% of the FIRST sources have such complex and extended morphology (Ivezić et al. 2002; Ching et al. 2017). Therefore, our cross-matching method can miss radio AGNs without a radio core and can misidentify radio lobes whose position matches an HSC-SSP source by chance.

3.2. Contamination and Completeness

Adopting a single search radius in the positional cross-match allows us to estimate the contamination and completeness of the source identifications in the following way. A total number of matches at $r_s < r'_s$ is represented by N_{tot} , where r'_s is an adopted search radius. The matches by chance coincidence at $r_s < r'_s$, N_{cc} , were estimated by the cross-match with the mock catalogs in the way mentioned in the previous section. The contamination is defined as the ratio of N_{cc} to N_{tot} . For convenience, we also defined a cleanliness that is defined as $(1 - \text{contamination})$. A number obtained by subtracting N_{cc} from N_{tot} is represented by N_A . We furthermore defined a number of matches, N_B , which is a number obtained by subtracting matches by chance coincidence at $r'_s < r_s < r''_s$ from the total number of matches in this radius range. We set r''_s of $2''.0$, where the completeness is assumed to be 100%. Finally, the completeness is defined as a ratio of N_A to a sum of N_A and N_B . In Figure 2, we show the cleanliness and completeness as a function of r_s for the Wide layer. The choice of the searching radius proved to be a reasonable trade-off between completeness and cleanliness of the sample. Indeed, at the adopted searching radius of $r_s \sim 1''.0$, the contamination by chance coincidence is estimated to be 14%, and the

Table 2
Summary of the Cross-matching Results

HSC Layer	HSC ^a	FIRST ^a	Match ^a	Matching Rate ^b	Area (deg ²)
Wide	23,795,523	7072	3579	0.506	154.09
UD-COSMOS	643,932	106	63	0.594	1.78

Notes.

^a The number of sources within the same effective area specified in the last column.

^b The matching rate is defined by a ratio of the number of matched sources to the number of FIRST sources.

completeness is estimated to be 93% in the Wide layer. In the UD-COSMOS, while the completeness is not well determined due to the small number of matches, the contamination is 16%.

The results of the cross-matches are summarized in Table 2. The cross-matches produced 3579 and 63 matched sources in the Wide and the UD-COSMOS layers, respectively. The matching rate, defined as the fraction of matched FIRST sources, is 51% in the Wide layer. The rate increases to 59% in the UD-COSMOS. Considering the above statistics, out of 3579 (63) matched HSC-FIRST sources in the Wide layer (UD-COSMOS), 3078 (53) are true optical counterparts of the FIRST sources, and 501 (10) FIRST sources are likely to be random matches. The estimated completeness implies that 3310 FIRST sources have HSC-SSP counterparts in the Wide layer, suggesting a completeness-corrected matching rate of 47%. These rates are higher than those of the previous studies using the SDSS ($\sim 30\%$; Ivezić et al. 2002; Helfand et al. 2015). The high matching rates with the HSC-SSP data are further discussed and compared with other studies in Section 5.3.

The matched HSC-FIRST samples of both the Wide and UC-COSMOS layers include no known pulsars in the ATNF pulsar catalog compiling all of the published rotation-powered pulsars (Manchester et al. 2005).

3.3. Extended Radio Sources

In order to evaluate a number of sources with extended radio morphology in the HSC-FIRST matched samples, we introduced a widely used size measure that is a ratio of the total integrated radio flux density to the peak radio flux density, or $F_{\text{int}}/F_{\text{peak}}$ (e.g., Ivezić et al. 2002; Schinnerer et al. 2007; Bondi et al. 2008; Smolčić et al. 2017a). The ratio $F_{\text{int}}/F_{\text{peak}}$ equals unity for a point source, while the ratio is larger than unity for an extended source or a resolved source. In Figure 3, we show the ratio as a function of the radio S/N. All the FIRST sources (gray dots), the HSC-FIRST sources in the Wide (blue dots), and the UD-COSMOS (yellow squares) are shown. The $F_{\text{int}}/F_{\text{peak}}$ values of less than 1.0 are due to their low S/N.

We consider that sources simultaneously meeting the following two criteria should be extended radio sources. The first one is a threshold line described by

$$\log(F_{\text{int}}/F_{\text{peak}}) = 0.1, \quad (1)$$

which was empirically determined for the FIRST-SDSS study by Ivezić et al. (2002), and sources above the line were classified as radio extended sources. This is, however, ineffective for the low-S/N sources. For a second criterion, we determined the lower envelope (the lower red curve) of the data points in Figure 3 following Schinnerer et al. (2007). The

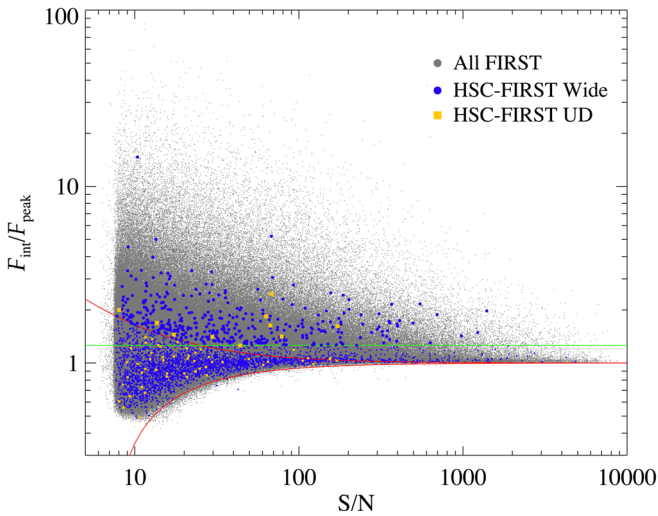


Figure 3. Ratio of the total flux density to the peak flux density as a function of the radio S/N. All of the FIRST sources are shown as gray dots. The HSC-FIRST matched sources in the Wide layer are indicated by blue dots, and those in the UD-COSMOS by yellow squares. The sources above the upper red curve and the green line are considered to be extended radio sources (see main text).

envelope contains 99% of all the FIRST sources below the $F_{\text{int}}/F_{\text{peak}} = 1$ line and was mirrored above $F_{\text{int}}/F_{\text{peak}} = 1$. The mirrored upper curve (the upper red curve) is represented as

$$F_{\text{int}}/F_{\text{peak}} = 1 + 6.5 \times (F_{\text{peak}}/\text{rms})^{-1}, \quad (2)$$

where $F_{\text{peak}}/\text{rms}$ is the S/N, and rms is a local rms noise in the FIRST catalog. Finally, we considered that the sources located above both the line of Equation (1) and the curve of Equation (2) should be radio extended sources in our samples.

Consequently, 10% (374 sources) of the HSC-FIRST Wide sample and 16% (10 sources) of the HSC-FIRST UD-COSMOS sample are selected to be radio extended sources. These extended sources are likely radio lobes matched by chance, FR-I RGs (Fanaroff & Riley 1974), RGs with core-jet/core-halo structures, or nearby star-forming galaxies. These fractions are thus upper limits of the numbers of chance coincidence of radio lobes, and the upper limits are compatible with the contaminations estimated in Section 3.1.

3.4. Optically Unresolved Sources

The optical morphologies on HSC images were examined to separate optically extended (resolved) sources and stellar-like unresolved objects using the procedure described in Akiyama et al. (2018) for distinguishing RGs and radio-loud quasars. We used a ratio of a second-order adaptive moment to that of a point-spread function at a source position. Because i -band images were taken under better conditions than the other bands, we use i -band images in this examination. The criteria for selecting stellar objects are

$$\begin{aligned} & \text{ishape_hsm_moments_11}/ \\ & \text{ishape_hsm_psfmoments_11} \\ & < 1.1, \end{aligned} \quad (3)$$

$$\begin{aligned} & \text{ishape_hsm_moments_22}/ \\ & \text{ishape_hsm_psfmoments_22} \\ & < 1.1. \end{aligned} \quad (4)$$

The suffixes of 11 and 22 represent each perpendicular axis in an image. We adopted the adaptive moments of the HsmMoments algorithm (Hirata & Seljak 2003). For 14 sources with failed HsmMoments measurements, the alternative adaptive moments of the SdssShape algorithm (Lupton et al. 2001) were adopted. According to Akiyama et al. (2018), the completeness of classified stellar objects in this classification decreases and the contamination from extended objects increases with increasing magnitude due to the misclassifications. At $i = 23$, the completeness is 80%–90%, and the contamination is less than 5%, while at $i > 24$, the completeness decreases down to $< 70\%$ and the contamination is more than 40%. Therefore, we consider that this classification of stellar objects is reliable for sources brighter than $i = 24$ mag.

According to the classification, we found 326 and 2 stellar objects from the HSC-FIRST Wide sample and the UD-COSMOS sample, respectively. These correspond to 9.1% and 3.2% of each sample, respectively. For brevity, we refer to such stellar objects as quasars and to optically resolved sources as RGs or galaxies, despite the recognition of exceptions to and uncertainties of the classification.

3.5. Astrometry

The large size of our sample provides us with an opportunity to inspect the astrometry between the HSC-SSP and FIRST sources. In Figure 4, we show the distributions of the residuals between the source positions of HSC-SSP and FIRST. The residuals along R.A. and decl. are a FIRST position minus an HSC-SSP position. We mention only results of the Wide layer because the UD-COSMOS sample is statistically too small to discuss the astrometry, but we just show the results of the UD-COSMOS sample.

The standard deviations of all the 3579 HSC-FIRST Wide sample are $0''.34$ in R.A. and $0''.37$ in decl. When we use only a bright and unresolved subsample whose sources are unresolved in radio morphology and have a radio peak flux of > 3 mJy and i magnitude of < 24 , the standard deviations slightly moderate down to $0''.26$ in R.A. and $0''.31$ in decl. These uncertainties are still large compared with the positional uncertainty of the HSC-SSP catalog ($0''.04$ against Pan-STARRS1; Aihara et al. 2018b) and slightly larger than the uncertainty of the FIRST catalog ($0''.2$ for bright and compact sources; White et al. 1997). This is likely due to the galaxies composing almost the entire HSC-FIRST sample; we do not limit the sample for this inspection only to optically unresolved objects because of its quite small sample size.

We found a mean offset in R.A. of $-0''.014 \pm 0''.006$ in all of the HSC-FIRST Wide sources. However, when we used only the bright and unresolved subsample, this systematic offset becomes $0''.004 \pm 0''.009$ and statistically not significant. On the other hand, the mean offset in decl. is $-0''.033 \pm 0''.006$ in the entire HSC-FIRST Wide sample. This offset is still significant and is $-0''.056 \pm 0''.011$, even if we use the bright and unresolved subsample. Therefore, there is a systematic offset in decl. of the HSC-SSP sources with respect to the FIRST position. Although this offset is significant, it is much smaller than the positional uncertainty of the FIRST catalog ($0''.2$), thus this offset has a negligible impact on the cross-match done in this work.

It may be valuable to compare the previous results of the FIRST sources with the SDSS counterparts studied by

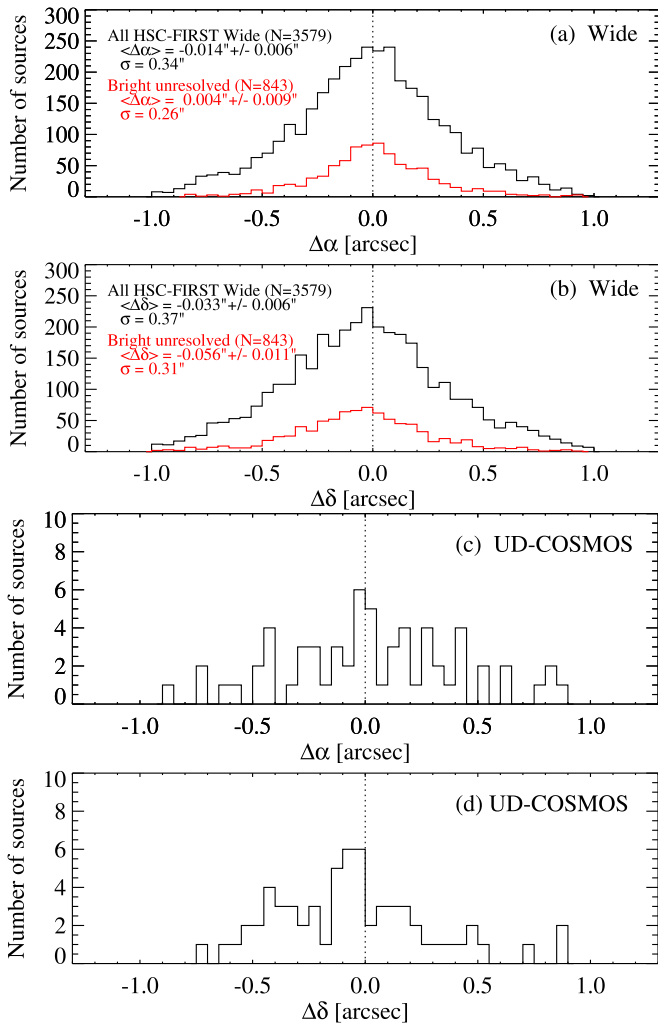


Figure 4. Separations ($\Delta\alpha$ and $\Delta\delta$) between an HSC position and a FIRST position in the Wide HSC-FIRST sample (the upper panels) and the UD-COSMOS sample (the lower). In the upper panels, the separations for all sources in the HSC-FIRST sample and the subsample of optically unresolved sources with $F_{\text{peak}} > 3$ mJy and $i < 24$ are shown as black and red lines, respectively.

Helfand et al. (2015). They reported that there are systematic offsets of $\sim 0''.02$ in R.A. and $\sim 0''.01$ in decl. of the FIRST positions with respect to both the SDSS sources and the FIRST sources that have been taken with the Karl G. Jansky Very Large Array (JVLA), which is a major upgrade of VLA. Hence, taking this previous result into consideration, there might also be offsets between HSC-SSP and SDSS. From this simple comparison, we inferred systematic offsets of $\sim 0''.02$ in R.A. and $\sim -0''.07$ in decl. from SDSS to HSC-SSP.

4. Radio and Optical Properties of HSC RGs

In this section, radio and optical properties of the HSC-FIRST matched samples are described. In particular, we investigate differences between RGs and radio-loud quasars, which were classified in Section 3.4. Moreover, we focus on differences between two subsamples: the optically faint HSC-FIRST sources (HSC-level), for which an optical counterpart is detected with HSC-SSP but is not with SDSS, and the optically bright HSC-FIRST sources (SDSS-level), for which an optical counterpart is detected both with HSC-SSP and SDSS.

4.1. Radio Source Counts

Radio properties of the Wide sample are investigated using 1.4 GHz radio source counts in Figure 5. Although radio source counts are often examined on a plane of radio flux and $(dN/dS)/S^{-2.5}$, we use another plane of radio AB magnitude and N to directly compare with the results of Ivezić et al. (2002). Here, the radio AB magnitude is expressed as

$$t [\text{AB mag}] = -2.5 \log(F_{\text{int}}/3631 \text{ Jy}). \quad (5)$$

A flux density of 1 mJy is equivalent to $t = 16.4$. In Figure 5, the source counts of the HSC-FIRST Wide sample, the Wide RG sample, and the Wide quasar sample are shown. Their distributions at a range of $11.5 < t < 15.5$ are fitted with a linear function by minimizing the chi-square statistic. The magnitude range for fitting is the same one as the analysis by Ivezić et al. (2002), whose results are also shown in Figure 5. The parameters of the best fits are summarized in Table 3.

The HSC-FIRST Wide sample (square) is roughly consistent with the FIRST sources whose SDSS counterparts are identified by Ivezić et al. (2002; the SDSS-FIRST sample, green solid line). This is trivial because the $\sim 20\%$ improvement of the matching rate in this study corresponds to an increase of only ~ 0.2 dex in $\log N/(\text{mag}^{-1} \text{ deg}^{-2})$ and a fact that FIRST sources without SDSS counterparts draw a similar slope to those with SDSS counterparts (Ivezić et al. 2002).

The HSC-FIRST quasars have a somewhat lower number than the SDSS-FIRST quasars, while the HSC-FIRST RGs increase in number, in particular, at the bright end. To investigate where this discrepancy stems from, we separate the HSC-FIRST Wide sample into an SDSS-level subsample with $i < 21.3$ and an HSC-level subsample with $i > 21.3$. The i magnitude threshold corresponds to the limiting magnitude of the SDSS survey, where the catalog is 95% complete for point sources (Stoughton et al. 2002). The 1.4 GHz radio source counts of the two subsamples and the fitting results are shown in Figure 6 and Table 3. The slope of the HSC-level RGs is flatter than that of the SDSS-level RGs, while the slope of the HSC-level quasars is steeper than that of the SDSS-level quasars. Therefore, the increased number of the HSC-FIRST RGs is likely due to the different dependences of the optically faint RGs and quasars from the optically bright sources on radio flux.

A fraction of quasars out of the SDSS-level subsample increases with increasing radio flux, from $\sim 20\%$ at the faint end to $\sim 60\%$ at the bright end. On the other hand, in the HSC-level subsample, the fraction does not strongly depend on radio flux. The fraction is approximately 5% over the radio flux range for fitting. The results in this subsection hold even if the HSC-level subsample is limited to sources with $i < 24$.

4.2. Optical Number Counts

Thanks to the depth of the HSC-SSP data, this study enables us to investigate optical properties of radio AGNs down to more than 3 mag fainter in brightness than previous SDSS studies. The i -band number counts of the HSC-FIRST Wide sample are shown in Figure 7. A fall-off of the HSC-FIRST Wide sample at the bright end ($i \lesssim 18$) is likely due to the saturation effect of the HSC-SSP data. A dearth of HSC-FIRST Wide quasars at the bright end is likely due to not only the saturation but also the rareness of radio-loud quasars. The SDSS radio-loud quasars are actually identified even at $i \lesssim 18$.

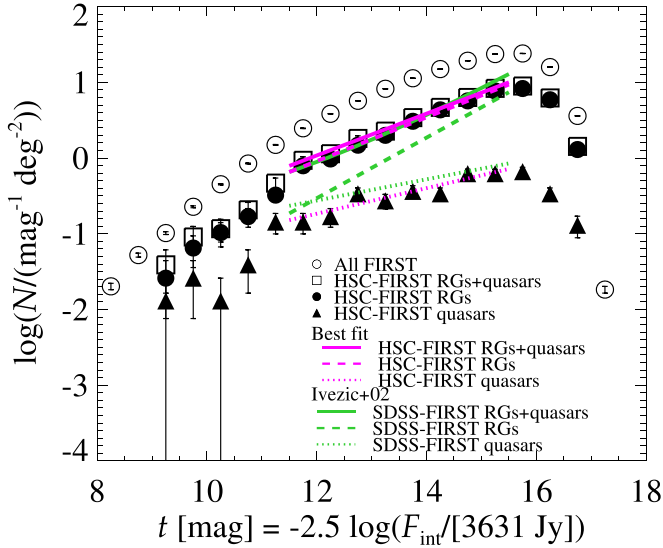


Figure 5. 1.4 GHz radio source counts of the HSC-FIRST Wide sample (square). The sample is separated into the HSC-FIRST RGs (filled circle) and the HSC-FIRST quasars (triangle). For comparison, all of the FIRST sources (open circle) are also shown. The 1.4 GHz flux density is converted to the equivalent AB magnitude, t . The Poisson errors in the data are indicated by vertical bars. The best fits for three HSC-FIRST samples in $11.5 < t < 15.5$ are overplotted (magenta lines). For comparisons, the distributions of the SDSS-FIRST samples (Ivezić et al. 2002) are shown as their best-fit lines (green lines). The SDSS-FIRST RG and quasar samples are morphologically classified subsets of optically resolved and unresolved sources out of the SDSS-FIRST sample, respectively. Both samples are limited to be brighter than 21 in r^* and have robust classifications. The SDSS-FIRST all sample is a combination of both the SDSS-FIRST RG and quasar sources, multiplied by 1.56 to retrieve the extracted sources by the $r^* < 21$ condition in the analysis by Ivezić et al. (2002). 64% sources meet their criteria.

(White et al. 2000; Ivezić et al. 2002). The i -band number counts of the SDSS radio-loud quasars overlap with those of the HSC-FIRST quasars around 18 mag (see Figure 7 in Ivezić et al. 2002). On the other hand, at the faint end at $i \gtrsim 25$, the number counts of the HSC-FIRST sources fall. The magnitude of this fall-off coincide with that of a fall-off for the HSC galaxy sample. Both fall-offs are considered to be due to the effect of the detection incompleteness of the HSC-SSP Wide data. It is presumed that the detection completeness is close to 100% down to brighter than ~ 24 mag because the i -band sources were detected with an S/N ratio of more than ~ 50 at $\lesssim 24$ mag. The number counts of the HSC-FIRST sources, which are not damped down to the detection completeness magnitude, implies a possibility that there are optically much fainter radio AGNs.

The number counts were fitted by a linear function within the $19 < i < 24$ range (magenta lines in Figure 7). The flat slope of the best fit for the HSC-FIRST RGs means that their number counts do not strongly depend on the apparent optical magnitude. The flat slope also indicates a decreasing fraction of the optically faint RGs relative to the HSC galaxies with increasing apparent magnitude: from 0.3% at $i = 19$ to 0.01% at $i = 24$. The small fraction of the faint RGs might imply a small number of distant RGs and/or RGs with a less massive host galaxy. For the HSC-FIRST quasars, there is a turnover at ~ 21 mag. Thus, the linear function is not well fitted to the data. The fraction to the HSC-FIRST sources drops off from 11% to $< 2\%$ over the turnover magnitude. This turnover appears at ~ 21 mag, and therefore, the turnover is not due to the detection completeness of HSC-SSP. The FIRST detection limit, in part,

Table 3
Fitting Results of 1.4 GHz Radio Source Counts

		a	b
All	RGs	$-3.51 (0.29)$	$0.289 (0.020)$
	quasars	$-2.76 (0.78)$	$0.169 (0.056)$
	RGs+quasars	$-3.28 (0.27)$	$0.276 (0.019)$
SDSS-level ($i < 21.3$)	RGs	$-4.82 (0.54)$	$0.348 (0.038)$
	quasars	$-1.99 (0.94)$	$0.102 (0.067)$
	RGs+quasars	$-3.99 (0.45)$	$0.296 (0.032)$
HSC-level ($i > 21.3$)	RGs	$-3.28 (0.35)$	$0.260 (0.024)$
	quasars	$-5.16 (1.79)$	$0.305 (0.123)$
	RGs+quasars	$-3.31 (0.34)$	$0.264 (0.024)$

Note. The best-fit parameters of the radio source counts in Figures 5 and 6. The fitting function is $\log(N/[mag^{-1} deg^{-2}]) = a + b t [AB mag]$. The numbers in the parentheses represent 1σ uncertainties in the fitting results.

Table 4
Fitting Results of the i -band Number Counts

	a	b
RGs	$-0.846 (0.276)$	$0.0617 (0.0127)$
quasars	$1.85^a (0.99)$	$-0.106^a (0.047)$
RGs+quasars	$-0.406 (0.261)$	$0.0436 (0.0120)$

Notes. The best-fit parameters of the i -band number counts in Figure 7. The fitting function is $\log(N/[mag^{-1} deg^{-2}]) = a + b i [AB mag]$. The numbers in the parentheses represent 1σ uncertainties in the fitting results.

^a The statistical significance of the fitting result for the quasars is apparently low.

may cause the turnover because the quasar sample misses optically faint radio-loud quasars with a lower radio flux than the FIRST detection limit. However, a similar turnover is not seen in the RG sample, although the effect of the FIRST detection limit should also impinge on the RG sample. This contrast means that the dependence of the number of quasars on optical magnitude is different from RGs in the optically faint regime. Jiang et al. (2007) found that the radio-loud fraction of quasars decreases with decreasing luminosity and increasing redshift although their quasar sample was basically brighter than $i = 18.9$. The turnover in our radio-loud quasar sample, therefore, may be partially attributed to a small number of low-luminosity radio-loud quasars and/or distant radio-loud quasars.

4.3. Radio Loudness

Radio loudness at the observed frame, \mathcal{R}_{obs} , is calculated to examine the radio activities of the HSC-FIRST RGs and quasars. According to Ivezić et al. (2002), \mathcal{R}_{obs} is defined as a ratio of the 1.4 GHz flux and i -band flux at the observed frames without k -corrections. The k -corrected radio loudness is discussed later (Section 5.1.3). The logarithmic \mathcal{R}_{obs} is described as

$$\log \mathcal{R}_{\text{obs}} = \log(F_{\text{int}}/F_i) = 0.4(i - t). \quad (6)$$

As mentioned in the introduction, the radio loudness could be underestimated for RGs, because the stellar light of a host galaxy is assumed to be dominant in the i -band flux.

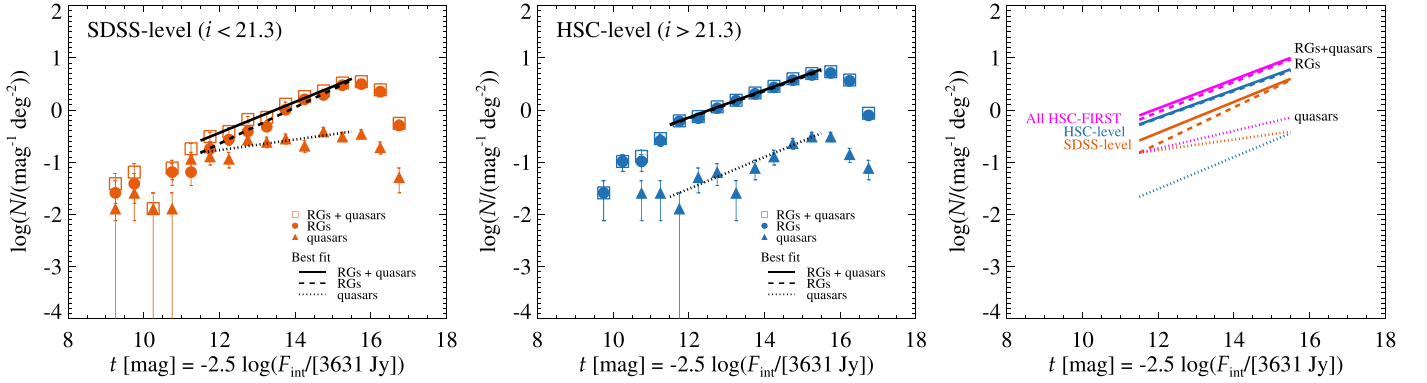


Figure 6. 1.4 GHz radio source counts of the optically bright subsample, SDSS-level (left panel), and the optically faint subsample, HSC-level (middle panel). See the text for details of the subsamples. Each subsample is further separated into RGs (circle) and quasars (triangle), which are classified by optical morphologies. The best-fit lines of each group are shown. The fit lines of the subsamples (orange lines for the SDSS level, blue lines for the HSC level) and those for all of the HSC-FIRST sources (magenta lines) are compared to each other (right panel). The fit lines for the RGs (broken lines) and quasars (dotted lines) of each sample are also indicated.

The \mathcal{R}_{obs} of the HSC-FIRST Wide and UD-COSMOS samples are shown in Figure 8. The HSC-FIRST samples obviously include higher \mathcal{R}_{obs} sources than the SDSS-level ones owing to the deep optical observations of HSC-SSP as we have expected. In particular, radio AGNs with more than $\log \mathcal{R}_{\text{obs}} = 3$ substantially increase in number. We note the \mathcal{R}_{obs} could be actually higher due to the underestimate by the contamination from host galaxies. Moreover, the \mathcal{R}_{obs} of the HSC-level sample is biased toward high values due to FIRST’s detection limit as illustrated by the green line in Figure 8. At the i -band magnitude range of the SDSS level, the quasars abound in the high \mathcal{R}_{obs} regime, whereas the RGs with high \mathcal{R}_{obs} are at the HSC-level range. The UD-COSMOS sample, as expected, includes optically fainter radio AGNs ($i \gtrsim 26$) than the Wide sample. However, despite the deeper depth of UD-COSMOS, the highest \mathcal{R}_{obs} radio AGNs are identified in the Wide layer. This means that wide optical surveys have an advantage over deeper but narrower surveys in finding rare AGNs such as the radio-loudest AGNs.

5. Discussion

5.1. Properties of HSC RGs as a Function of Photometric Redshift

We have successfully identified a large number of the optically faint optical counterparts of FIRST radio sources thanks to the wide and deep HSC-SSP survey. We reported in the previous section that these optically faint FIRST sources show apparently high radio loudness. In this section, we further investigate the optical and radio properties of the optically faint FIRST sources in order to understand their nature. We use the photometric redshift (photo- z or z_{photo}) of the sample but quasars have large uncertainties in photo- z ; therefore, we address only RGs other than quasars.

5.1.1. Color–Color

The redshifts of the HSC-FIRST RG samples in both the Wide and UD-COSMOS layers are examined in a color–color plane as the first step. Our RG samples are shown in the $r - i$ and $i - z$ color–color diagram of Figure 9. As the selection criteria have been imposed on the HSC-FIRST sample to detect in these three bands of r , i , and z , the three bands’ photometries are available for all of the HSC-FIRST sources. The colors were compared with two color tracks of two model galaxies

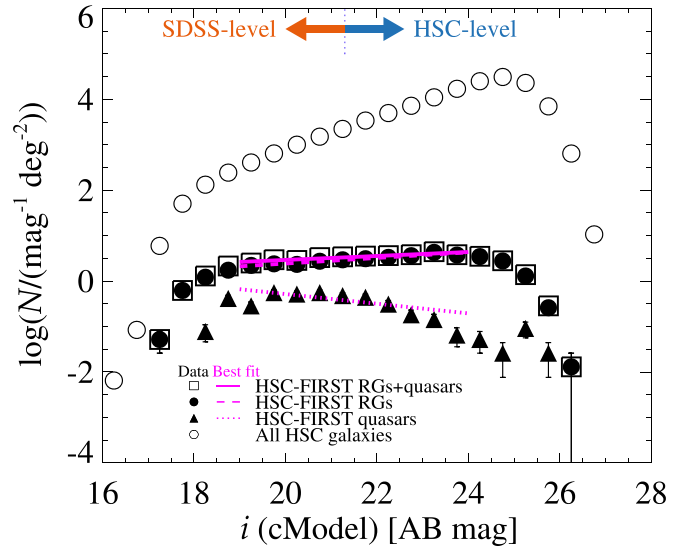


Figure 7. Optical HSC i -band number counts of the HSC-FIRST samples. The symbols are the same as Figure 5 but the circle indicates all of the HSC galaxies. The best fits are also shown by magenta lines for the HSC-FIRST Wide, Wide RGs, and Wide quasar samples.

(Bruzual & Charlot 2003) in order to estimate their redshifts. One is a passive elliptical galaxy that has star formation history with an exponential decay time of 1 Gyr, a galaxy age of 8 Gyr, and the solar metallicity. The other is a star-forming galaxy that has an instantaneous burst, a galaxy age of 0.025 Gyr, and the solar metallicity. From Figure 9, we found that most of the sources are located along the track of the model elliptical galaxy from $z \sim 0$ to $z \sim 1$.

5.1.2. Photometric Redshifts

Photo- z estimated using the Mizuki SED-fitting code and the photometries of the five HSC-SSP bands (see Tanaka 2015; Tanaka et al. 2018 for details) are available for our HSC-FIRST RG sample. A total of 2714 RGs in the Wide layer and 49 RGs in the UD-COSMOS layer have reliable photo- z , where $z_{\text{photo}} > 0$, 2σ error in z_{photo} ($2\sigma_{z_{\text{photo}}}$) is less than 1, and a reduced χ^2 less than 5. The photo- z sample does not have a systematic bias against the optical magnitudes of sources at $i < 24$. On the other hand, $\sim 30\%$ of the faint HSC-FIRST RGs with $i > 24$ are not included in the photo- z sample due to the

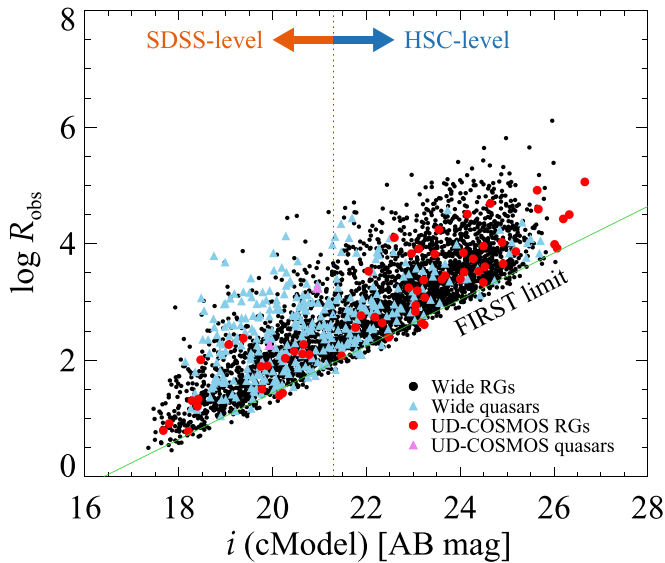


Figure 8. Logarithmic radio loudness $\log \mathcal{R}_{\text{obs}}$ at the observed frame as a function of HSC i -band magnitude. The RGs and quasars in the Wide sample are indicated by black circles and light blue triangles, respectively. Of the UD-COSMOS sample, the RGs and quasars are shown as red circles and violet triangles, respectively. The green line indicates the detection limit of FIRST point sources. The blue dotted line is the border separating the SDSS-level and HSC-level samples by their i -band magnitude.

low reliability of their photo- z . This bias results in a lack of 36% among RGs with $\log \mathcal{R}_{\text{obs}} > 5$. The redshifts of the photo- z sample are shown in Figure 10 and range from $z_{\text{photo}} \sim 0$ to ~ 1.5 in both the Wide and UD-COSMOS layers. The apparent bimodal distribution with two peaks at $z_{\text{photo}} \sim 0.6$ and 1.2 could be attributed to both a spiky photo- z distribution of the parent HSC sample (see Figure 11 in Tanaka et al. 2018) and a rapid decrease of the photo- z objects toward $z_{\text{photo}} \sim 1.7$ where the five HSC bands can no longer straddle a redshifted 4000 Å break. The interval of the spiky photo- z distribution is roughly 0.1 and is smaller than the average uncertainties (0.2) in the photo- z of the photo- z sample. The photo- z distributions of the SDSS-level and HSC-level RGs are clearly divided into low and high redshifts, respectively. This result means that the optically faint RGs or the HSC-level RGs (~ 1500 sources) exist at high redshifts ($\gtrsim 1$) rather than at the local universe as intrinsically optically faint objects.

In order to inspect the photo- z for validity, the photo- z were compared with spectroscopically measured redshifts (spec- z or z_{spec}) when available. We used public spec- z catalogs from SDSS DR12 (Alam et al. 2015), GAMA DR2 (Liske et al. 2015), VIPERS PDR1 (Garilli et al. 2014), VVDS (Le Fèvre et al. 2013), WiggleZ DR1 (Drinkwater et al. 2010), PRIMUS DR1 (Coil et al. 2011; Cool et al. 2013), and zCOSMOS DR3 (Lilly et al. 2009). We cross-matched the public spec- z sources to the HSC-FIRST photo- z sources in positions by a $1''.0$ search radius. Of the HSC-FIRST photo- z sample, 404 RGs in the Wide layer and 11 RGs in the UD-COSMOS have secure spec- z where $z_{\text{spec}} > 0$, an error in z_{spec} greater than 0, and a secure homogenized quality flag of z_{spec} determinations (see Tanaka et al. 2018 for details). The optical magnitudes of the spec- z sample are limited to be $i < 21.8$ due to the magnitude limit of the spectroscopic observations. In Figure 11, the photo- z and the spec- z are compared each other. The means and standard deviations of the relative differences between both are $(z_{\text{photo}} - z_{\text{spec}})/(1 + z_{\text{spec}}) = -0.015 \pm 0.057$ for the Wide

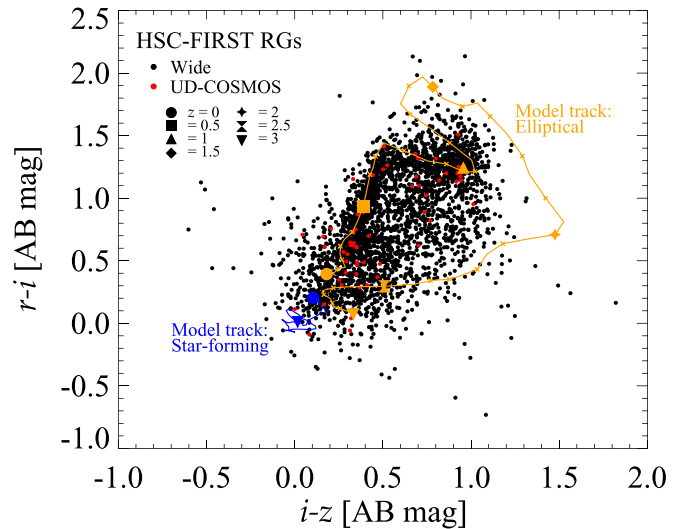


Figure 9. Color-color diagram of $r - i$ and $i - z$. The HSC-FIRST Wide RGs and UD-COSMOS RGs are shown as black circles and red circles. To estimate their redshifts, color tracks of two model galaxies are overplotted: a passive elliptical galaxy (orange curve) and a star-forming galaxy (blue curve). Each redshift of a model track is marked by large filled symbols (see the inserted legends). To be eye friendly, minor ticks indicated by small crosses show $\Delta z = 0.1$ steps. Only $z = 0$ and 3 marks are shown in the star-forming galaxy track.

sources and -0.017 ± 0.012 for the UD-COSMOS sources. In the overall trend, the photo- z is in good agreement with spec- z for the $i < 21.8$ sources.

In order to examine the photo- z of the faint sources with $i > 22.0$, we utilized the photo- z (z_{L16}) of the COSMOS2015 catalog in the COSMOS field, which were estimated using 30 multiband photometric data from the ultraviolet to the mid-infrared (Laigle et al. 2016). The UD-COSMOS photo- z RG subsample includes 44 counterparts of the COSMOS2015 sources with the minimum reduced χ^2 of the SED fitting being less than 5. In Figure 12, the relative differences between z_{photo} and z_{L16} for 44 matched RGs are shown as a function of z_{L16} . Both photo- z are consistent with each other within 10% up to $z_{\text{L16}} \sim 1.7$. The standard deviation of the relative difference is 0.047 in $z_{\text{L16}} < 1.7$. At $z_{\text{L16}} > 1.7$, where the sources are fainter than $i \sim 24$, the relative difference is systematically negative and is -30% at the most. This deviation at $z_{\text{L16}} > 1.7$ is attributed to a redshifted 4000 Å break beyond the y -band, and therefore, the photo- z of these sources cannot be accurately constrained only from the photometries of the five HSC-SSP bands. These examinations show that the HSC-SSP photo- z could be secure, at least, at $z_{\text{photo}} \lesssim 1.7$, although the photometric sensitivities of the UD-COSMOS layer are deeper than those of the Wide layer.

5.1.3. Optical and Radio Properties

The optical luminosity and radio luminosity at the rest frame were calculated using the photo- z for the photo- z subsample. In Figure 13, the calculated luminosities are shown as a function of photo- z . The 1.4 GHz radio luminosity was k -corrected by assuming a power-law radio spectrum of the form $\propto \nu^\alpha$ with index $\alpha = -0.7$ (e.g., Condon 1992). The sources at $z \gtrsim 1$ have high 1.4 GHz luminosities compared with lower redshift sources due to a bias from the FIRST sensitivity. The rest-frame g -band absolute magnitude was estimated by the SED template fitting Mizuki (Tanaka 2015; Tanaka et al. 2018).

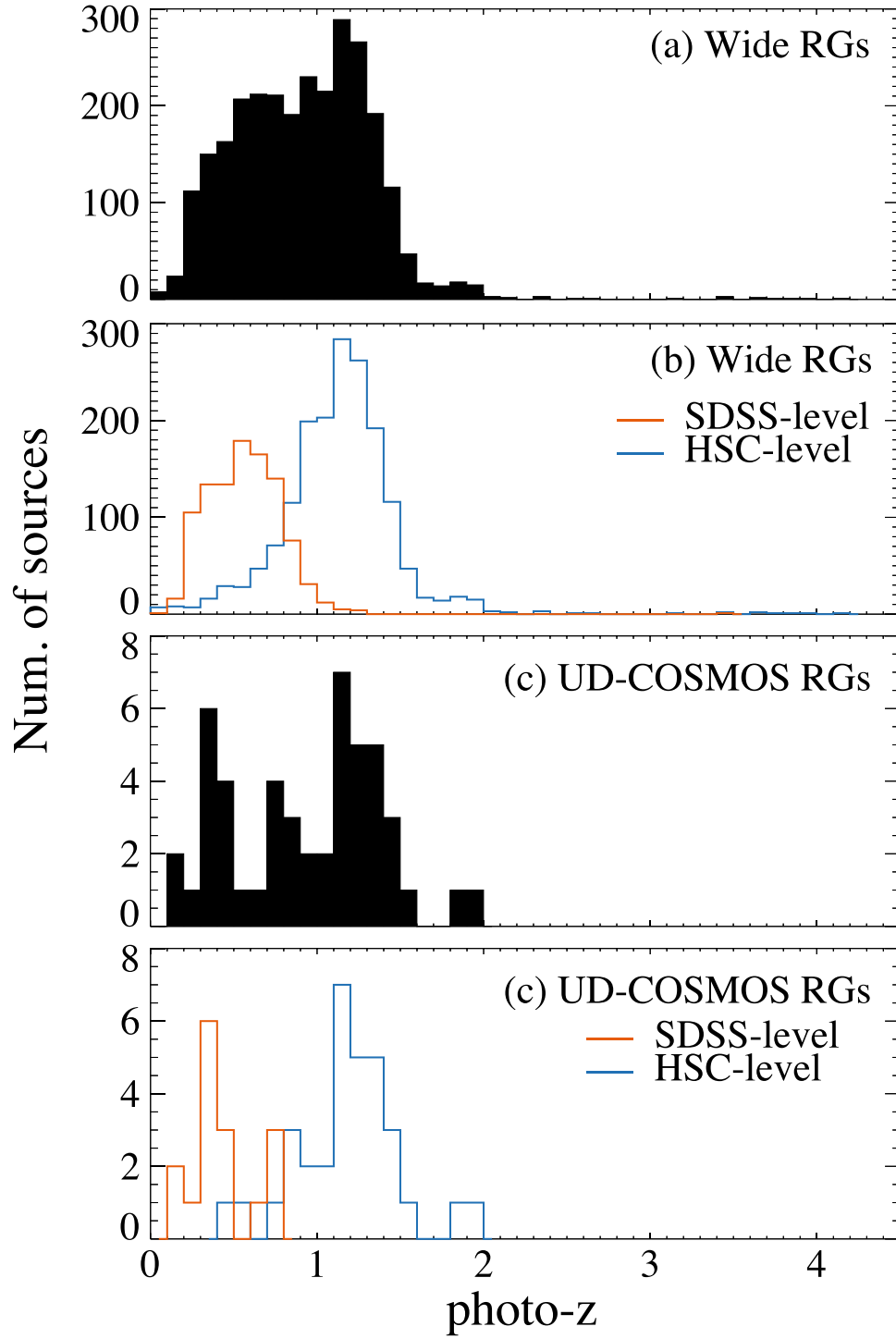


Figure 10. Histograms of photometric redshifts. The RGs in the Wide (a) and the UD-COSMOS (c) layers are shown by black bars. The RGs in both layers are separated into the SDSS level (orange) and the HSC level (blue) in panels (b) and (d). Only RG sources with the reliable photometric redshifts, with $z_{\text{photo}} > 0$, $2\sigma_{z_{\text{photo}}} < 1$, and $\chi^2_{\nu} < 5$, are shown.

There may be two sequences of the g magnitude along the redshifts. The bright sequence with $M_g \lesssim -21$ does not strongly depend on the redshift. On the other hand, the number of sources belonging in the faint sequence seems to dramatically increase with increasing redshifts. The sources with faint absolute magnitudes are also faint in apparent magnitudes ($i > 24$), and the optical SEDs of the HSC-SSP bands show that some sources on the faint sequence have a flat SED without distinct features. Thus, the redshifts of these

sources are probably estimated incorrectly. In fact, the comparison of M_g and redshifts with the COSMOS2015 catalog (Laigle et al. 2016) in UD-COSMOS shows the underestimated redshifts of the faint sequence sources, and the redshifts of COSMOS2015 indicate that most sources in the faint sequence should be at $z_{\text{L16}} > 1.5$. In this comparison, a source at $z = 0.5$ on the faint sequence was found to have redshift and M_g consistent with the COSMOS2015 catalog. This source is really a local source with a faint optical

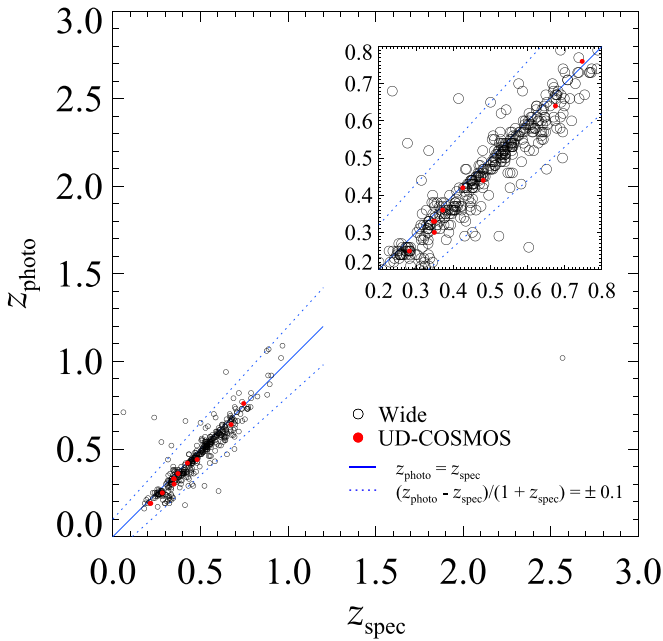


Figure 11. Comparison between the photo- z and spec- z of the HSC-FIRST RGs ($i < 22.0$) with reliable photo- z and spec- z . The sources in the Wide (black circles) and UD-COSMOS (red circles) are shown. The solid line represents $z_{\text{photo}} = z_{\text{spec}}$. The dotted lines of $(z_{\text{photo}} - z_{\text{spec}})/(1 + z_{\text{spec}}) = \pm 0.1$ serve as a guide to the eye. The inserted figure shows plots at a redshift range of 0.2–0.8.

luminosity. The faint sequence could be an apparent one due to both the effects of the underestimated redshifts and the Malmquist bias of the HSC-SSP sensitivity limits. Some sources at $z \lesssim 0.5$ may be local galaxies with strong radio radiation from active star formation.

Radio loudness at the rest frame was estimated and is defined here as a ratio of the rest-frame 1.4 GHz flux to the rest-frame g -band flux. The wavelength of the rest-frame g -band flux is close to the rest-frame B -band, which is typically used for calculating the radio loudness. The rest-frame radio loudnesses of the SDSS- and HSC-level sources as a function of the apparent i -band magnitude are shown in Figure 14. We found that RGs with high radio loudness ($\log R_{\text{rest}} > 3$) are found in the HSC-level subsample. Certainly, there are likely also low radio-loudness RGs in the HSC-level regime, but such sources are not included due to the sensitivity limit of the FIRST survey. Note that the radio loudness we use here is underestimated, because HSC band flux could be dominated by stellar light from host galaxies of RGs, and the rest-frame g -band flux is derived from the SED templates of galaxies.

We show each distribution of the SDSS- and HSC-level RG samples in an $R_{\text{rest}} - z_{\text{photo}}$ plane in Figure 15. We distinctly found that the optically faint RGs (the HSC level) have higher radio loudnesses and photo- z than the optically bright RGs (the SDSS level). Again, we note that optically faint RGs with a low radio loudness are not detected due to the FIRST sensitivity. However, we claim that our HSC-FIRST RG sample includes a large number (~ 730) of the optically faint RGs that have high radio loudness ($\log R_{\text{rest}} > 3$) and redshifts of more than 1. These RGs have not been probed by SDSS.

5.2. Optical Spectra and Quasar/Galaxy Classification

We performed a quasar/galaxy classification using optical spectra in order to inspect the morphological classification

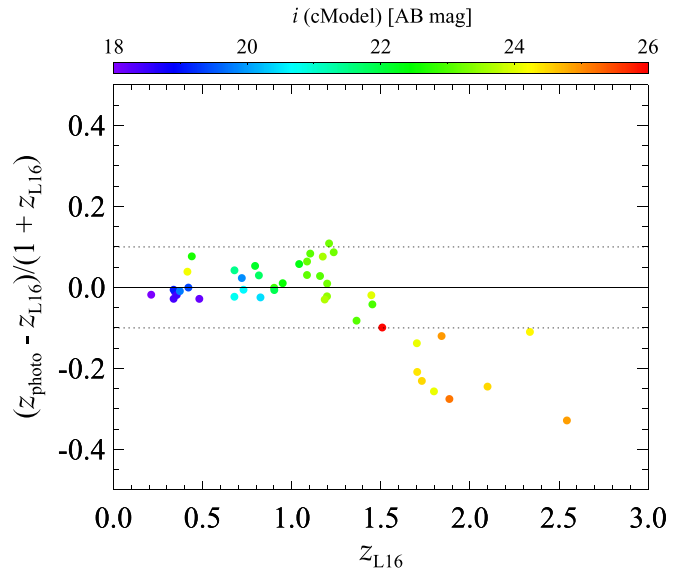


Figure 12. Relative difference between the HSC-SSP photo- z (z_{photo}) and the photo- z in the COSMOS2015 catalog (z_{L16} , Laigle et al. 2016). The plotted data are the photo- z sources in the UD-COSMOS, which have secure photo- z in both catalogs (see text). The colors of the data indicate the i -band magnitude of the sources according to the color bar at the top of the figure. The solid line represents $z_{\text{photo}} = z_{\text{L16}}$ and the dotted lines $(z_{\text{photo}} - z_{\text{L16}})/(1 + z_{\text{L16}}) = \pm 0.1$ as a guide to the eye.

based on the HSC-SSP images in Section 3.4. This inspection is based on whether or not a spectrum of a source that was morphologically classified as a quasar (or a galaxy) shows broad emission lines. We used archival spectra available from SDSS DR12 (Alam et al. 2015), GAMA PDR2 (Liske et al. 2015), and zCOSMOS (Lilly et al. 2009). In addition to the archival spectra, we also examined 18 spectra that have been recently obtained with 2dF-AAOmega installed on the 3.9 m Anglo-Australian Telescope (AAT) in 2017 July. See W. He et al. (2018, in preparation) for details about the observation and data reduction. Finally, we inspected 622 sources in the Wide layer and 21 in the UD-COSMOS layer. These subsamples include sources without a secure spec- z . Although this spectral inspection allows us to confirm the morphological classification using the HSC-SSP images, we should take into account the following two points. One is that the i -band magnitudes of these subsamples are biased toward a bright side and are distributed from 17.4 to 22.8 in the Wide layer and from 17.7 to 21.9 in UD-COSMOS. The other is that this spectral inspection does not distinguish between quasars and broad-line RGs.

Of the 622 Wide sources with available spectral classification, we have 152 morphologically classified quasars and 470 galaxies. The inspection results show that 130 (86%) morphologically classified quasars and 26 (5.5%) morphologically classified galaxies show broad emission lines. In UD-COSMOS, 2/2 (100%) morphologically classified quasars and 1/19 (5.3%) morphologically classified galaxies show broad emission lines. Therefore, at $i \lesssim 23$, there could be 5% contaminations of quasars in both the morphologically classified RG samples of the Wide layer and UD-COSMOS. Examples of four types of spectra, a quasar with/without broad emission lines and a galaxy with/without broad emission lines, are shown in Figure 16.

Additionally, we inspected a redshift dependence of the success rate of the morphological classification with the HSC

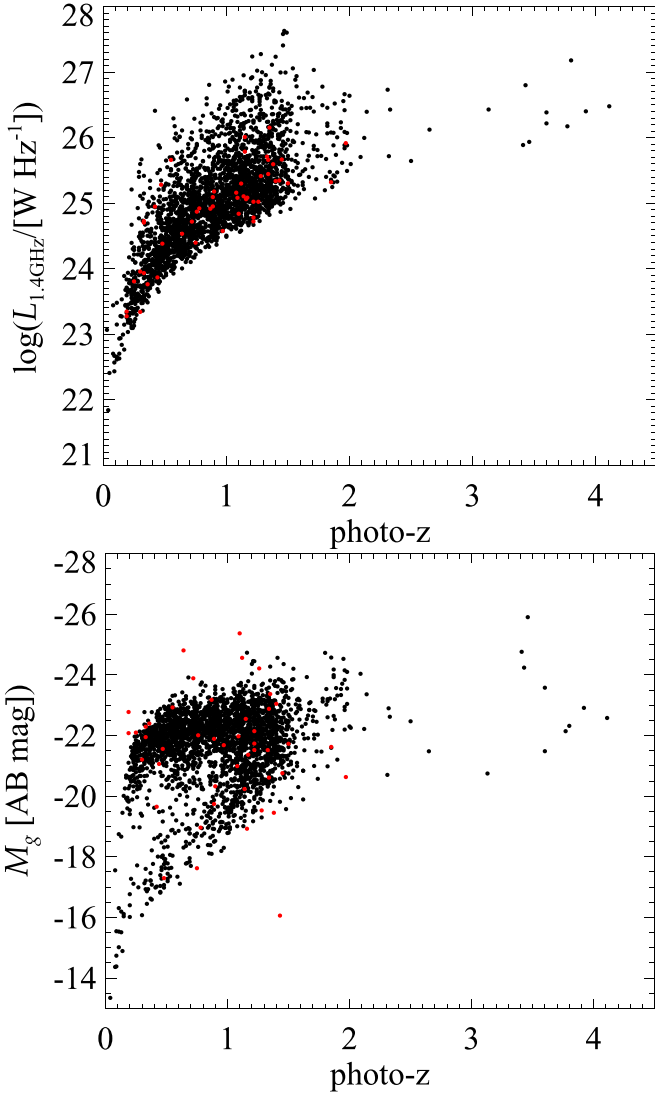


Figure 13. Rest-frame 1.4 GHz radio luminosity (upper panel) and the absolute g -band magnitude at the rest frame (lower panel) as a function of photo- z . Only RG sources with reliable photometric redshifts, with $z_{\text{photo}} > 0$, $2\sigma_{z_{\text{photo}}} < 1$, and $\chi^2_\nu < 5$, are shown. The black circles and red circles denote the Wide and UD-COSMOS RGs, respectively.

images. In the classification, an RG could be misclassified as a radio-loud quasar when a source is at a high redshift. We used the morphological information measured with the Advanced Camera for Surveys (ACS) on the *Hubble Space Telescope* (*HST*) in the COSMOS region (Leauthaud et al. 2007) and our morphological classification with simulated HSC images at the Wide layer depth in UD-COSMOS. This inspection employed *HST* ACS morphology data and HSC UD-COSMOS at an imaging depth equivalent to the Wide-layer depth. The ACS images have a higher spatial resolution ($0''.12$) than the HSC Wide layer and thus provide a robust classification. The HSC UD-COSMOS images at the Wide layer depth provide three types of seeing: best, median, and worst seeing images with FWHMs of $0''.5$, $0''.7$, and $1''.0$, respectively (Aihara et al. 2018b). The success rate of the HSC morphological classification is defined as a fraction of a number of sources classified as a galaxy by both ACS and HSC to a number of sources classified as a galaxy by ACS. The success rate was examined up to $z_{\text{photo}} = 2$ as presented in Figure 17. We confirmed the

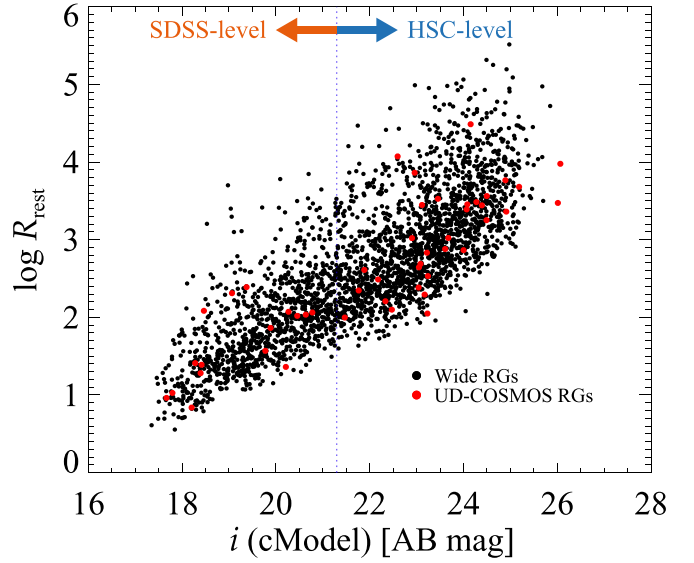


Figure 14. Radio loudness at the rest frame as a function of the apparent i -band magnitude. The RG sources with reliable photo- z in the Wide (black) and the UD-COSMOS (red) layers are shown. The blue dotted line is the border separating the SDSS-level and HSC-level samples by their i -band magnitude.

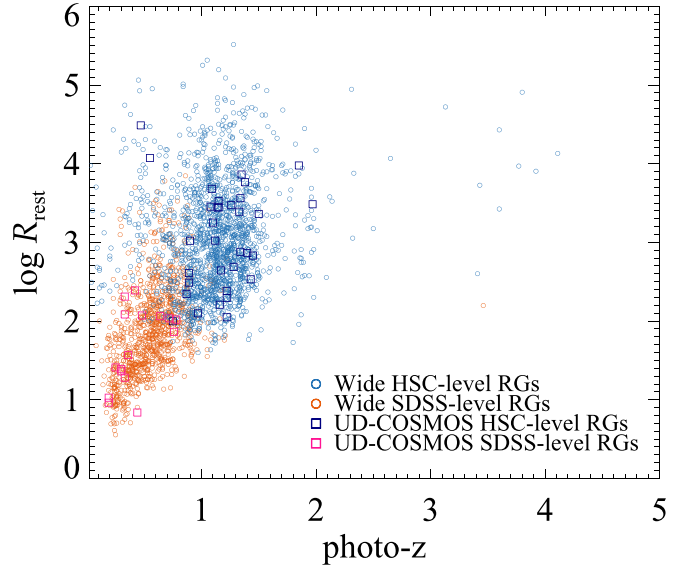


Figure 15. Radio loudness at the rest frame as a function of photo- z . Only the RG sources with reliable photo- z are shown. Sources at the SDSS-level and the HSC-level brightness in the Wide layer (UD-COSMOS) are represented by blue circles (dark blue squares) and orange circles (pink squares), respectively.

redshift dependence of the success rate, which moderately decreases with redshifts. The success rate is 95%–97% at $z_{\text{photo}} > 1$ in the median seeing. Therefore, we found that 3%–5% of RGs at $z_{\text{photo}} > 1$ could be radio-loud quasars.

5.3. Improved Matching Rate

Our study using the Subaru HSC-SSP catalog has successfully identified the optical counterparts of 51% and 59% of the FIRST sources in the HSC-SSP Wide layer and UD-COSMOS, respectively. These matching rates are significantly higher than the $\sim 30\%$ matching rates of the SDSS-based studies by Ivezić

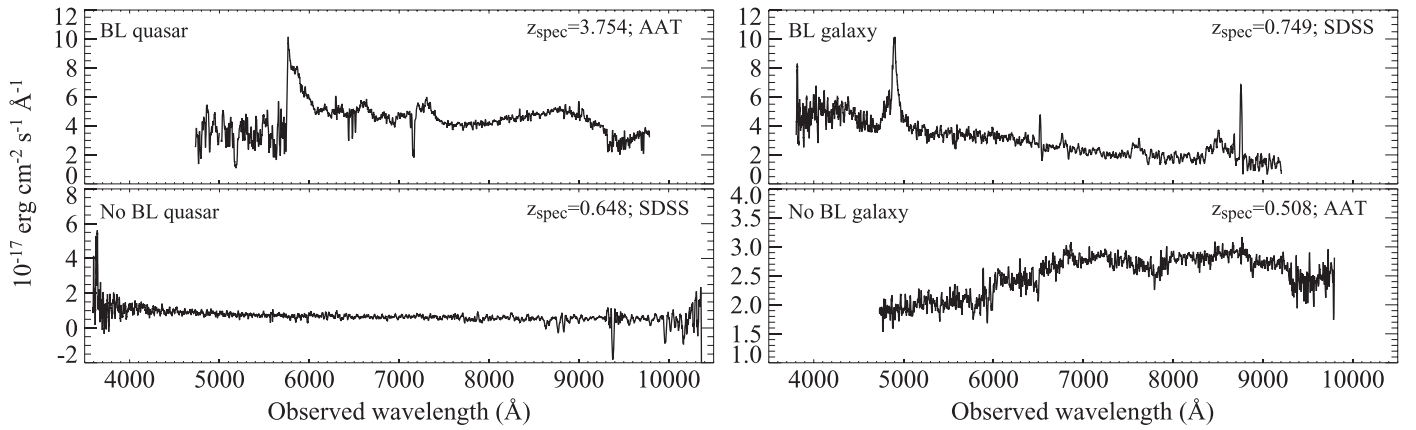


Figure 16. Examples of optical spectra of HSC-FIRST sources. Four types of spectra are shown: a morphologically classified quasar with broad emission lines (top left), a morphologically classified galaxy with broad emission lines (top right), a morphologically classified quasar without broad emission lines (bottom left), and a morphologically classified galaxy without broad emission lines (bottom right). Two spectra were obtained with AAT (W. He et al. 2018, in preparation) and others were taken from SDSS DR12.

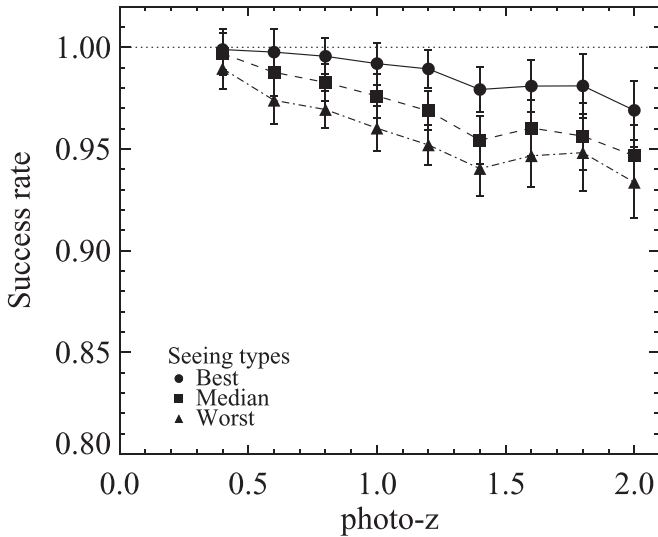


Figure 17. Success rate of the HSC morphological classification of galaxy/quasar as a function of redshift. The success rate is defined as the fraction of sources classified as a galaxy by both *HST*/ACS and HSC to the number of sources classified as a galaxy by *HST*/ACS. Three types of seeing in the HSC images are shown: best (FWHM $\sim 0''.5$, circle), median ($\sim 0''.7$, square), and worst ($\sim 1''.0$, triangle). The error bars represent the Poisson errors.

et al. (2002), Helfand et al. (2015), and Ching et al. (2017). Although the adopted search radii are different between the studies, even if we use the completeness-corrected matching rate, our result (47% in the Wide layer) is still higher than the corrected rate of 31% in Ivezić et al. (2002). It is clear that the improved matching rate is due to the utilization of the deep optical catalog, compared with the previous studies, from Figures 7, 8, and 14. This interpretation is supported by the higher matching rate of 59% in UD-COSMOS, which has fainter HSC-SSP sources than the Wide layer.

However, approximately 40% of FIRST sources in the HSC-SSP unmasked region still have no optical counterparts within $1''$ of their positions. Our sample criterion of $S/N > 5$ in r , i , and z likely misses a certain fraction of HSC-SSP sources with an extremely red color at the faint end, such as high- z red galaxies. Other unmatched FIRST sources are roughly grouped into two types from the inspections of their HSC-SSP images.

The first consists of radio sources with bright radio companion (s) close to it. These sources are likely radio lobes associated with low- z RGs. The second consists of single radio components. These optical counterparts may be extremely faint in the optical ($i < 26$), such as radio AGNs with a quite low accretion rate, obscured AGNs, radio AGNs in less massive host galaxies, or high-redshifted objects.

6. Summary

We presented the results of the exploration of radio AGNs using the Subaru HSC-SSP catalog and the FIRST VLA catalog. This is the initial result of an ongoing project, WERGS. The positional cross-match between HSC-SSP and FIRST produced 3579 and 63 optical counterparts of the FIRST radio sources in the Wide layer and UD-COSMOS, respectively. These numbers of the matched counterparts correspond to more than 50% of the FIRST radio sources in the search fields, showing a much higher matching rate than the previous studies of optically bright SDSS-FIRST sources ($i < 21$).

We reported the properties in the optical and radio wavelengths of the matched HSC-FIRST sources. Among the HSC-FIRST sources, 9% in the Wide and 3% in the UD-COSMOS layers are optically unresolved sources, that is, likely radio-loud quasars. The i -band number counts show a flat slope down to 24 mag, implying a constant number of either less massive or distant radio AGNs. The optically faint sources show the different slopes of the 1.4 GHz source counts from the bright sources with $i < 21.3$. Almost all of the photometric redshifts of the subsample with available redshift data range up to 1.5. In particular, the optically faint sources are distributed around the redshift of 1. The comparison of the color-color diagram with the galaxy model also shows a similar redshift distribution to the photometric one, and most of the sources are consistent with redshifted early-type galaxies although there is a large dispersion. Thanks to the deep and wide HSC-SSP survey, we found a large number (~ 730) of sources with high radio loudness ($\log R > 3$) in the optically faint regime. Such sources are distributed at $z \gtrsim 1$.

We also showed that rare objects such as sources with the highest radio loudness are found in the wide and shallow field (the Wide layer) rather than in the small and deep field (UD-COSMOS). Together with the improved matching rates, these

results demonstrated the advantages of our project over previous radio AGN searches in terms of both optical depth ($i < 26$) and the wide search field (more than 150 deg^2).

We would like to thank the anonymous referee for very useful comments that helped to further improve this paper. This work is based on data collected at the Subaru Telescope and retrieved from the HSC data archive system, which is operated by the Subaru Telescope and Astronomy Data Center at the National Astronomical Observatory of Japan.

The Hyper Suprime-Cam (HSC) collaboration includes the astronomical communities of Japan and Taiwan, and Princeton University. The HSC instrumentation and software were developed by the National Astronomical Observatory of Japan (NAOJ), the Kavli Institute for the Physics and Mathematics of the Universe (Kavli IPMU), the University of Tokyo, the High Energy Accelerator Research Organization (KEK), the Academia Sinica Institute for Astronomy and Astrophysics in Taiwan (ASIAA), and Princeton University. Funding was contributed by the FIRST program from the Japanese Cabinet Office, the Ministry of Education, Culture, Sports, Science and Technology (MEXT), the Japan Society for the Promotion of Science (JSPS), Japan Science and Technology Agency (JST), the Toray Science Foundation, NAOJ, Kavli IPMU, KEK, ASIAA, and Princeton University.

This paper makes use of software developed for the Large Synoptic Survey Telescope. We thank the LSST Project for making their code available as free software at <http://dm.lsstcorp.org>.

The Pan-STARRS1 Surveys (PS1) have been made possible through contributions of the Institute for Astronomy, the University of Hawaii, the Pan-STARRS Project Office, the Max Planck Society and its participating institutes, the Max Planck Institute for Astronomy, Heidelberg, and the Max Planck Institute for Extraterrestrial Physics, Garching, The Johns Hopkins University, Durham University, the University of Edinburgh, Queen's University Belfast, the Harvard-Smithsonian Center for Astrophysics, the Las Cumbres Observatory Global Telescope Network Incorporated, the National Central University of Taiwan, the Space Telescope Science Institute, the National Aeronautics and Space Administration under grant No. NNX08AR22G issued through the Planetary Science Division of the NASA Science Mission Directorate, the National Science Foundation under grant No. AST-1238877, the University of Maryland, and Eotvos Lorand University (ELTE)

Based in part on data acquired through the Australian Astronomical Observatory, under program A/2017A/008. We acknowledge the traditional owners of the land on which the AAT stands, the Gamilaraay people, and pay our respects to elders past and present.

The National Radio Astronomy Observatory is a facility of the National Science Foundation operated under cooperative agreement by Associated Universities, Inc.

This work is financially supported by the Japan Society for the Promotion of Science (JSPS) KAKENHI 16H01101, 16H03958, and 17H01114 (T.N.). Y.M. was supported by the Japan Society for the Promotion of Science (JSPS) KAKENHI Grant No. JP17H04830 and the Mitsubishi Foundation Grant No. 30140.

Facilities: Subaru (HSC), VLA.









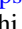

Software: STILTS (Taylor 2006), IDL, IDL Astronomy User's Library (Landsman 1993), TOPCAT (Taylor 2005).

Appendix Counting FIRST Sources on the Unmasked HSC-SSP Regions

In order to count the number of FIRST sources on the unmasked HSC-SSP regions, we have to consider the FIRST sources lying within the masked HSC-SSP regions that result from the selection of the clean HSC-SSP sample. The flags in the masked regions are described in mask images through an integer bitmask value (see Bosch et al. 2018 for details). Regions with the following bitmasks are considered as masked regions corresponding to the sample selection criteria described in Section 2.1: BAD (a sensor defect), BRIGHT_OBJECT (a region near a very bright object), CR (a cosmic ray), EDGE (the edge of a CCD or coadded patch), INTRP (an interpolated pixel), SAT (a saturated pixel), and SUSPECT (a pixel value above the level where the linearity correction is reliable).

There were originally 8282 (118) FIRST sources in the HSC-SSP Wide layer (UD-COSMOS) defined in Table 1 before any masks were performed. These numbers were FIRST sources that have the nearest HSC-SSP sources within $20''$ for the purpose of excluding FIRST sources on the patches with poor photometries (see Section 2.1) and counting FIRST sources in UD-COSMOS. After masking, we obtained 7072 and 106 FIRST sources in the unmasked regions of the Wide layer and UD-COSMOS, respectively.

ORCID iDs

Takuji Yamashita  <https://orcid.org/0000-0002-4999-9965>
Tohru Nagao  <https://orcid.org/0000-0002-7402-5441>
Masayuki Akiyama  <https://orcid.org/0000-0002-2651-1701>
Wanqiu He  <https://orcid.org/0000-0001-7759-6410>
Hiroyuki Ikeda  <https://orcid.org/0000-0002-1207-1979>
Masayuki Tanaka  <https://orcid.org/0000-0002-5011-5178>
Masaru Kajisawa  <https://orcid.org/0000-0002-1732-6387>
Tomoki Morokuma  <https://orcid.org/0000-0001-7449-4814>
Yoshiki Toba  <https://orcid.org/0000-0002-3531-7863>
Akotoki Noboriguchi  <https://orcid.org/0000-0002-5197-8944>

References

- Aihara, H., Arimoto, N., Armstrong, R., et al. 2018a, *PASJ*, 70, S4
- Aihara, H., Armstrong, R., Bickerton, S., et al. 2018b, *PASJ*, 70, S8
- Akiyama, M., He, W., Ikeda, H., et al. 2018, *PASJ*, 70, S34
- Alam, S., Albareti, F. D., Allende Prieto, C., et al. 2015, *ApJS*, 219, 12
- Becker, R. H., White, R. L., & Helfand, D. J. 1995, *ApJ*, 450, 559
- Bock, D. C.-J., Large, M. I., & Sadler, E. M. 1999, *AJ*, 117, 1578
- Bondi, M., Ciliegi, P., Schinnerer, E., et al. 2008, *ApJ*, 681, 1129
- Bosch, J., Armstrong, R., Bickerton, S., et al. 2018, *PASJ*, 70, S5
- Bruzual, G., & Charlot, S. 2003, *MNRAS*, 344, 1000
- Ching, J. H. Y., Sadler, E. M., Croom, S. M., et al. 2017, *MNRAS*, 464, 1306
- Ciliegi, P., Zamorani, G., Bondi, M., et al. 2005, *A&A*, 441, 879
- Coil, A. L., Blanton, M. R., Burles, S. M., et al. 2011, *ApJ*, 741, 8
- Condon, J. J. 1992, *ARA&A*, 30, 575
- Condon, J. J., Cotton, W. D., Greisen, E. W., et al. 1998, *AJ*, 115, 1693
- Cool, R. J., Moustakas, J., Blanton, M. R., et al. 2013, *ApJ*, 767, 118
- Coupon, J., Czakon, N., Bosch, J., et al. 2018, *PASJ*, 70, 7
- Drinkwater, M. J., Jurek, R. J., Blake, C., et al. 2010, *MNRAS*, 401, 1429
- Edge, D. O., Shakeshaft, J. R., McAdam, W. B., Baldwin, J. E., & Archer, S. 1959, *MmRAS*, 68, 37
- Fabian, A. C. 2012, *ARA&A*, 50, 455
- Fanaroff, B. L., & Riley, J. M. 1974, *MNRAS*, 167, 31P

- Furusawa, H., Koike, M., Takata, T., et al. 2018, *PASJ*, **70**, S3
- Garilli, B., Guzzo, L., Scodreggio, M., et al. 2014, *A&A*, **562**, A23
- He, W., Akiyama, M., Bosch, J., et al. 2018, *PASJ*, **70**, S33
- Helfand, D. J., White, R. L., & Becker, R. H. 2015, *ApJ*, **801**, 26
- Hirata, C., & Seljak, U. 2003, *MNRAS*, **343**, 459
- Intema, H. T., Jagannathan, P., Mooley, K. P., & Frail, D. A. 2017, *A&A*, **598**, A78
- Ivezić, Ž., Menou, K., Knapp, G. R., et al. 2002, *AJ*, **124**, 2364
- Jiang, L., Fan, X., Ivezić, Ž., et al. 2007, *ApJ*, **656**, 680
- Kellermann, K. I., Sramek, R., Schmidt, M., Shaffer, D. B., & Green, R. 1989, *AJ*, **98**, 1195
- Komiyama, Y., Obuchi, Y., Nakaya, H., et al. 2018, *PASJ*, **70**, S2
- Laigle, C., McCracken, H. J., Ilbert, O., et al. 2016, *ApJS*, **224**, 24
- Landsman, W. B. 1993, in ASP Conf. Ser. 52, adass II, ed. R. J. Hanisch, R. J. V. Brissenden, & J. Barnes (San Francisco, CA: ASP), 246
- Le Fèvre, O., Cassata, P., Cucciati, O., et al. 2013, *A&A*, **559**, A14
- Leauthaud, A., Massey, R., Kneib, J.-P., et al. 2007, *ApJS*, **172**, 219
- Lilly, S. J., Le Brun, V., Maier, C., et al. 2009, *ApJS*, **184**, 218
- Liske, J., Baldry, I. K., Driver, S. P., et al. 2015, *MNRAS*, **452**, 2087
- Lupton, R., Gunn, J. E., Ivezić, Z., Knapp, G. R., & Kent, S. 2001, in ASP Conf. Ser. 238, adass X, ed. F. R. Harden, Jr., F. A. Primini, & H. E. Payne (San Francisco, CA: ASP), 269
- Manchester, R. N., Hobbs, G. B., Teoh, A., & Hobbs, M. 2005, *AJ*, **129**, 1993
- McCarthy, P. J. 1993, *ARA&A*, **31**, 639
- McNamara, B. R., Nulsen, P. E. J., Wise, M. W., et al. 2005, *Natur*, **433**, 45
- Miley, G., & De Breuck, C. 2008, *A&ARv*, **15**, 67
- Miyazaki, S., Komiyama, Y., Kawanomoto, S., et al. 2018, *PASJ*, **70**, S1
- Morganti, R., Fogasy, J., Paragi, Z., Oosterloo, T., & Orienti, M. 2013, *Sci*, **341**, 1082
- Schinnerer, E., Smolčić, V., Carilli, C. L., et al. 2007, *ApJS*, **172**, 46
- Schlegel, D. J., Finkbeiner, D. P., & Davis, M. 1998, *ApJ*, **500**, 525
- Seymour, N., Stern, D., De Breuck, C., et al. 2007, *ApJS*, **171**, 353
- Simpson, C., Martínez-Sansigre, A., Rawlings, S., et al. 2006, *MNRAS*, **372**, 741
- Simpson, C., Rawlings, S., Ivison, R., et al. 2012, *MNRAS*, **421**, 3060
- Smolčić, V., Delvecchio, I., Zamorani, G., et al. 2017a, *A&A*, **602**, A2
- Smolčić, V., Novak, M., Bondi, M., et al. 2017b, *A&A*, **602**, A1
- Stoughton, C., Lupton, R. H., Bernardi, M., et al. 2002, *AJ*, **123**, 485
- Tadhunter, C. 2016, *A&ARv*, **24**, 10
- Tanaka, M. 2015, *ApJ*, **801**, 20
- Tanaka, M., Coupon, J., Hsieh, B.-C., et al. 2018, *PASJ*, **70**, S9
- Taylor, M. B. 2005, in ASP Conf. Ser. 347, adass XIV, ed. P. Shopbell, M. Britton, & R. Ebert (San Francisco, CA: ASP), 29
- Taylor, M. B. 2006, in ASP Conf. Ser. 351, adass XV, ed. C. Gabriel et al. (San Francisco, CA), 666
- White, R. L., Becker, R. H., Gregg, M. D., et al. 2000, *ApJS*, **126**, 133
- White, R. L., Becker, R. H., Helfand, D. J., & Gregg, M. D. 1997, *ApJ*, **475**, 479
- Williams, W. L., Calistro Rivera, G., Best, P. N., et al. 2018, *MNRAS*, **475**, 3429
- York, D. G., Adelman, J., Anderson, J. E., Jr., et al. 2000, *AJ*, **120**, 1579